Scattering of Polarized Laser Light by Water Droplet, Mixed-Phase and Ice Crystal Clouds. Part I: Angular Scattering Patterns

KENNETH SASSEN AND KUO-NAN LIOU

Department of Meteorology, University of Utah, Salt Lake City 84112

(Manuscript received 17 October 1978, in final form 15 January 1979)

ABSTRACT

Laboratory studies of the angular scattering and depolarizing behavior of water, ice and mixed-phase clouds are described in Parts I and II of this report. In Part I, we present the theoretical background and experimental apparatus for determining the angular scattering pattern in the laboratory. The experimental results obtained with vertically and horizontally polarized laser light (0.6328 μm) are given in the form of normalized scattering phase functions to facilitate their comparison to theoretical predictions. Close agreement between Mie theory and experiment is found for water clouds when the measured cloud droplet size distribution is input into the computations. For ice crystal clouds containing small (<50 μm), randomly oriented particles, the agreement with theory using either the spherical or long cylinder shape approximation is less noteworthy due to the presence of more intense side-scattering and the absence of cloudbows in the experimental ice data. The scattering behavior of mixed-phase clouds, an important group of atmospheric clouds, is shown to be highly sensitive to the differences in the relative scattering efficiencies of the water and ice particles as a function of the scattering angle. Also considered are the effects of ice crystal size and shape on the angular scattering patterns. Finally, normalized phase function values for a representative ice crystal cloud are presented in tabulated form.

1. Introduction

Knowledge of the angular scattering behavior of atmospheric clouds is of great importance to the quantitative treatment of the transfer of radiation through the atmosphere. Such information also has major implications for the determination of cloud composition by means of passive and active remote sensing techniques. In order to perform realistic radiation transfer calculations, the cloud-layer composition must be categorized and the appropriate angular scattering pattern applied for this model of cloud content. The angular scattering behavior of water droplet clouds may be precisely specified from the Mie theory for a representative polydispersion of homogeneous water spheres. For clouds containing ice crystals, however, determination of the angular scattering behavior is still an area requiring further study. Due to the lack of a rigorous theoretical solution to the scattering of light by particles with the arbitrary geometry of ice crystals, experimental findings must be relied on for the present to characterize the scattering properties of ice clouds and assess the validity of approximate theoretical approaches to this problem.

The results of previous studies utilizing approximate theoretical solutions (Jacobowitz, 1970; Liou, 1972) and laboratory measurements (Huffman and Thursby, 1969; Huffman, 1970; Dugin *et al.*, 1971, 1977; Liou *et al.*, 1976; Sassen and Liou, 1978) have revealed that ice crystals scatter considerably more energy into the side-scatter region than "equivalent" assemblies of cloud droplets, a finding that appears to be valid in general for particles of irregular shape (Holland and Gagne, 1970). This increased side-scattering efficiency is indicated to take place at the expense of ice crystal scattering in both the forward and backward directions. Although measurements near the 0° and 180° scattering angles have not been obtained in the experimental studies, monostatic lidar (Platt, 1973) and continuous-wave laser (Sassen, 1978a) observations have indeed shown considerably lower backscattering efficiencies for ice crystal clouds.

Several areas of uncertainty remain regarding the utilization of the angular scattering patterns for the computation of radiation transfer through the cloudy atmosphere. A problem shared by both the theoretical and experimental attempts is in accounting for the scattering and polarization properties of the various shapes of ice crystals which occur naturally. The scattering behavior of mixed-phase clouds which are encountered frequently in the real atmosphere should also receive attention.

What is clearly needed to obtain this information is a comprehensive experimental program under controlled laboratory conditions. As a first step in such a program, experimental results obtained from artificial water, mixed-phase and ice clouds are reported

0022-4928/79/050838-14$07.50

here in Parts I and II. The experimental angular scattering patterns in the parallel polarization plane are compared to theoretical scattering computations using spherical and cylindrical particle shapes in Part I. The observations and remote sensing significance of the angular depolarizing behavior of the clouds are reported in Part II (Sassen and Liou, 1979). Before giving the experimental results, we begin our discussion with a review of the theoretical foundation for the determination of the angular scattering phase functions, and then describe the experimental apparatus utilized in this study.

2. Theoretical considerations

In the construction of the polar nephelometer, the transmitter and receiver have been arranged in such a way that the scattered light is measured in a fixed horizontal plane with polarizers both parallel and orthogonal to the incident polarization plane. Hence, the Stokes parameters of the scattered light in units of radiance may be written as (Liou, 1975)

$$\mathbf{I}(\theta)=C\mathbf{M}(\theta)\mathbf{F}_0, \tag{1}$$

where C is a constant of proportionality, and the incident light in units of flux density is given by

$$\mathbf{F}_0=\begin{bmatrix} F_{0l} \\ F_{0r} \\ U_0 \\ V_0 \end{bmatrix}, \tag{2}$$

with l and r representing polarization components in the horizontal and vertical directions, respectively. Generally, if no assumptions are made concerning the physical positions of nonsymmetrical particles in space, the phase matrix contains 16 independent parameters.

Ice crystals generated in the laboratory cold chamber are normally relatively small, and as a consequence tend to orient randomly in space. Under these circumstances, if we assume that a plane of symmetry is created, then the number of independent phase-matrix elements is reduced to six (Perrin, 1942; van de Hulst, 1957). Thus, we have

$$\mathbf{M}(\theta)=\begin{bmatrix} M_{11} & M_{12} & 0 & 0 \\ M_{12} & M_{22} & 0 & 0 \\ 0 & 0 & M_{33} & M_{34} \\ 0 & 0 & -M_{34} & M_{44} \end{bmatrix}. \tag{3}$$

If horizontally polarized light is used as the incident radiation source, then the scattered radiance is given by

$$\mathbf{I}=CF_{0l}\begin{bmatrix} M_{11} \\ M_{12} \\ 0 \\ 0 \end{bmatrix}. \tag{4}$$

For incident vertically polarized radiation, on the other hand, the scattered radiation is

$$\mathbf{I}'=CF_{0r}\begin{bmatrix} M_{12} \\ M_{22} \\ 0 \\ 0 \end{bmatrix}. \tag{5}$$

Note that M_{12} in Eqs. (4) and (5) represents the depolarized components, which, in principle, has the same magnitude for horizontally or vertically polarized incident light with the plane of symmetry assumption.

For spherical water droplets, the number of independent phase-matrix elements is further reduced to four. The phase matrix may be expressed by

$$\mathbf{M}(\theta)=\begin{bmatrix} M_{11} & 0 & 0 & 0 \\ 0 & M_{22} & 0 & 0 \\ 0 & 0 & M_{33} & M_{34} \\ 0 & 0 & -M_{34} & M_{33} \end{bmatrix}. \tag{6}$$

Thus, the scattered radiances for water clouds corresponding to Eqs. (4) and (5) are, respectively,

$$\mathbf{I}=CF_{0l}\begin{bmatrix} M_{11} \\ 0 \\ 0 \\ 0 \end{bmatrix}, \tag{7}$$

$$\mathbf{I}'=CF_{0r}\begin{bmatrix} 0 \\ M_{22} \\ 0 \\ 0 \end{bmatrix}. \tag{8}$$

It is clear that if scattering measurements are made with a receiver in the planes of polarization parallel and orthogonal to that of the transmitter on a fixed plane, the depolarized components from linearly polarized incident light would be zero for spherical water droplets. Based on the measured angular depolarized components from water clouds it follows that we may investigate the strength of multiple scattering as a function of the scattering angle, as will be examined in Part II. Finally, we define the normalized

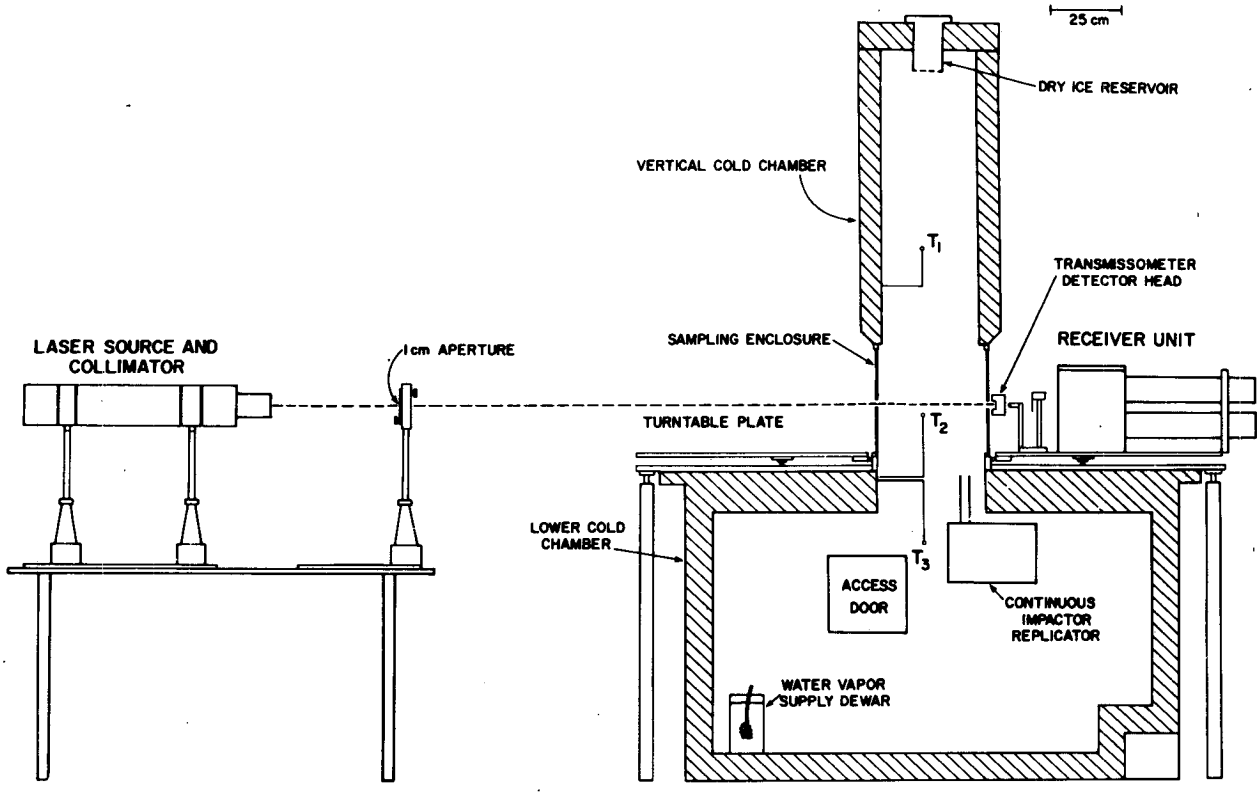

FIG. 1. The experimental system for the determination of the angular light scattering properties of artificial clouds. This side view shows the polarized light from the rotable laser source incident from the left. That portion of the laser light scattered by cloud particles in the horizontal plane is measured as a function of the scattering angle as the receiver unit revolves around the sampling enclosure between the two cold chambers.

nondimensional phase-matrix elements as

$$P_{ij}(\theta)/4\pi = M_{ij}(\theta)/2\pi \int_0^{\pi} M_{ij}(\theta) \sin\theta d\theta,$$

$$i, j = 1, 2, 3, 4. \quad (9)$$

3. The experimental arrangement

a. The experimental configuration and technique

The experimental system is basically a polar nephelometer for the determination of angular scattering patterns (in the horizontal plane) from laboratory cloud particle assemblies which are restricted to a central sampling region in order to avoid immersing the entire apparatus in the cloud. The cloud particles are confined to the central region by means of a cylindrical enclosure (0.3 m diameter) located at the junction between a large rectangular cold chamber and a vertical cold chamber or "chimney," which in combination generate the artificial clouds (see Fig. 1). The receiver unit is fixed to a turntable which revolves at a constant rate about the central enclosure. The light beam from the stationary laser source is passed through the center of the cylindrical sampling enclosure by means of a semi-circular slit through which the receiver also views the cloud. A viewing tube for the receiver is attached to the turntable and extends slightly through the observation slit, which is otherwise sealed with two strips of foam insulation. A laser power meter detector head mounted behind the laser beam exit point (i.e., at the 0° scattering angle) is used to monitor fluctuations in cloud transmission which can be related to cloud composition variations.

The light source used in these experiments is a He-Ne laser (0.6328 μm) with a highly linearly polarized output of 5.2 mW. A laser collimator is used to increase the beam diameter to 1 cm and to reduce beam divergence to <1 mrad. In order to generate both vertical and horizontal incident polarizations the laser is mounted in a specially designed rotatable fixture with mechanical stops at the vertical and horizontal positions.

Shown in Fig. 2 is the receiver design which enables the vertical and horizontal polarization plane components to be simultaneously measured. The receiver field-of-view is defined by two pinholes with 1.72 mm diameters, with the scattering volume delineated by the volume of intersection between this field-of-view and the laser beam at various observation angles. The diameter of the receiver field-of-view at the intersection with the laser beam is equal to the laser

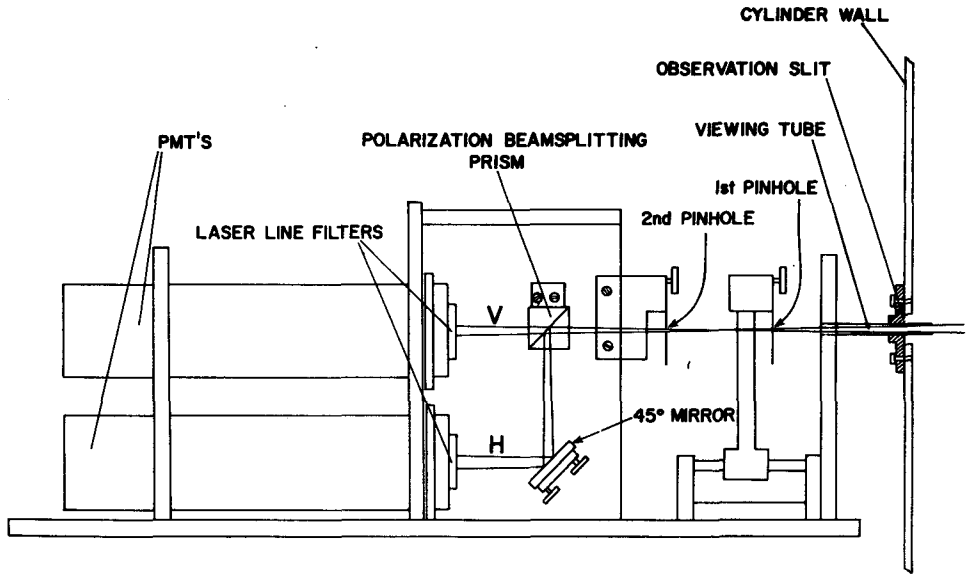

FIG. 2. The components of the receiver unit which define the cloud scattering volume and allow for the simultaneous measurement of the laser light scattered in the vertical (V) and horizontal (H) planes of polarization.

beam diameter. The scattered light admitted through the pinholes is passed through a Glan-Thompson polarizing prism which divides the incident energy into two orthogonal, linearly polarized components. The vertically polarized component is directly admitted into the top photomultiplier tube (PMT), with the horizontally polarized component being reflected into the bottom PMT with a 45° plane mirror. Both photodetectors are equipped with 1.0 nm bandpass laser line interference filters.

The photodetectors used in these experiments are two RCA 7265 PMT's with extended S-20 bi-alkali photocathodes whose gains were absolutely calibrated. The signals from the photomultiplier tubes are amplified by Keithly Model 417 Picoammeters which display favorable bandwidth, dynamic range and dark current suppression capabilities for this application. The outputs from the picoammeters are then directed to X-Y recorders for recording the orthogonal components of the phase functions. A dual-channel strip-chart recorder is used to continuously monitor cloud transmissivity from the calibrated detector head signal (in watts) and the air temperature from one of three locations in the cold chambers, as shown in Fig. 1.

Due to the presence of the transmissometer detector head and the receiver configuration, the system design ordinarily permits data collection from scattering angles of 10° (from the forward, incident direction) to 165° (in the backward direction). For the experiments described here, two 45° mirrors have been used to direct the laser beam into the chamber so that backscattering angles of up to 175° can be viewed by the receiver. The time sweeps of the X-Y recorders and the turntable motor drive are initiated by a clock at the main control panel and are terminated by a motor control stop switch when the angular scan is completed. The scans are typically completed in 3.5 min.

b. Artificial cloud production and sampling

Artificial water clouds are generated in the cold chamber through the use of a vessel containing distilled water and an immersion heating element. The record of the laser beam transmission through the cloud is used to identify stable water cloud conditions. It is then possible to initiate successive scattering scans of the stable water clouds, or to seed the cloud with dry ice, liquid nitrogen or silver iodide agents to generate ice crystals. It is also possible to gradually reintroduce cloud droplets into the scattering volume following cloud glaciation by adjusting the water reservoir heating rate and seeding materials supply.

To measure the microphysical composition of the artificial clouds for the important comparison to the scattering data, a cloud sampling device is positioned in the lower chamber $\sim$25 cm below the scattering volume and operated at intervals during the experiments. The design and operation of this device, the Continuous Impactor Replicator especially developed for laboratory cloud chamber applications, is described thoroughly in Sassen (1978b). With this device, cloud samples are collected by impaction onto a freshly Formvar solution-coated substrate in order to preserve the size and shape of the particles in a thin plastic layer for later microscopic examination. The substrate on which the permanent particle casts are preserved is transparent 35 mm film leader which travels at high speeds under the impactor jet during each 5 s

sampling interval. The time of each sample is notated in the continuous strip-chart recorder data for reference to the scattering scans.

c. Scattering data analysis

To reduce the recorded scattering data, the scans are divided into 5° scattering angle intervals and the relative scattered intensity values $I(\theta)$, in amperes, are derived by averaging the recorded signal deflections over each 5° interval. The absolute scattered power $P_s(\theta)$ can then be derived as a function of scattering angle from

$$P_s(\theta)=I(\theta)G_r, \tag{10}$$

where G_r is the gain of the receiver channels (in units of watts per ampere) and includes the transmissivities of the interference filters at the laser line frequency.

The basic parameter of the experimental angular scattering pattern is the volume scattering coefficient $\beta_s(\theta)$ [m^{-1} sr^{-1}] as a function of the scattering angle. This value can be derived from the scattered power measurements using the following analog of the lidar equation:

$$P_s(\theta)=\frac{P_i}{A_b}\frac{V(90°)}{\sin\theta}\omega_r\beta_s(\theta)\exp(-\sigma' R), \tag{11}$$

where P_i is the incident (linearly polarized) laser power measured prior to cloud formation, A_b the cross-sectional area of the laser beam in the scattering volume, $V(90°)$ the scattering volume at $\theta=90°$ (0.68 cm^3), ω_r the solid angle of light scattered from a particle which is viewed by the receiver, integrated over the scattering volume (10^{-5} sr), and where the exponential term accounts for the "apparent" attenuation of the laser beam after traversing the cloud. The first two terms define the laser power density and the change in the scattering volume with angle, respectively. The last term yields only an approximation of the true attenuation from Beer's law in which all scattering (note that absorption by cloud particles is negligible in our case) is removed from the propagating beam. However, in the experiments, the laser power measurement P_r after the beam has traversed the cloud actually includes energy scattered along the beam from diffraction and multiple scattering due to the finite width of the detector aperture. Thus, we define the "apparent" extinction coefficient σ' [m^{-1}] in terms of total cloud pathlength R as

$$\sigma'=-\frac{1}{R}\ln\frac{P_r}{P_i}. \tag{12}$$

Note that the approximate cloud optical thickness τ' can be found by simply multiplying the σ' values by the total cloud length R of 0.3 m.

For dense laboratory clouds, the above procedure underestimates the true attenuation. However, the use of the apparent attenuation in the determination of β_s values is considered appropriate since the scattered energy remaining in the beam contributes to further scattering, in effect, increasing the incident energy available for scattering. Then substituting Eq. (12) into (11) now yields the simplified expression

$$\beta_s(\theta)=\frac{P_s(\theta)A_b\sin\theta}{P_r\omega_r V(90°)}. \tag{13}$$

In the data to be presented here, the angular scans of β_s are converted into phase function values in order to facilitate their comparison to Mie scattering results, and adjust for cloud microphysical differences to improve the intercomparison of the scans. The normalized scattering phase function $P(\theta)$ is derived from the experimental data using the expression

$$P(\theta)/4\pi=\beta_s(\theta)/2\pi\int_{\theta_1}^{\theta_2}\beta_s(\theta)\sin\theta d\theta, \tag{14}$$

where θ_1 and θ_2 are scattering angles $\theta_1=10°$ and $\theta_2=175°$ which correspond to the angular termination of the scans.

It should be noted that the use of (14) produces phase functions which are shifted to higher values (as in Figs. 8 and 10), primarily as a result of the neglect of the 0–10° interval where, for example, as much as about one-half of the scattered energy may be concentrated for a representative cloud droplet size distribution. Therefore, where spherical particles are involved (Figs. 3 and 12), or where direct comparisons of ice data are made to theoretical phase functions (Fig. 6 and Table 1), the experimental data are adjusted by computing the normalized phase function for a population of spheres with the same size distribution as that measured and scaling the experimental values to correspond with the theoretical values at $\theta=10°$. The use of this procedure for ice cloud data may be justified with the knowledge that forward scattering is governed largely by diffraction in which particle shape effects are relatively unimportant, so that randomly oriented irregular particles may be treated with "equivalent" spheres. As pointed out by van de Hulst (1957), the average geometric cross section of randomly oriented particles is equal to one-quarter of the particle surface area. Hence, it can be shown that the relation between the maximum dimensions of ice crystals and the diameter of spheres with equivalent surface area varies with the crystal diameter-to-thickness ratio, and that no significant errors should result unless very thin or long crystals are involved.

Concerning sources of errors in the β_s values, measurement errors may result primarily from the im-

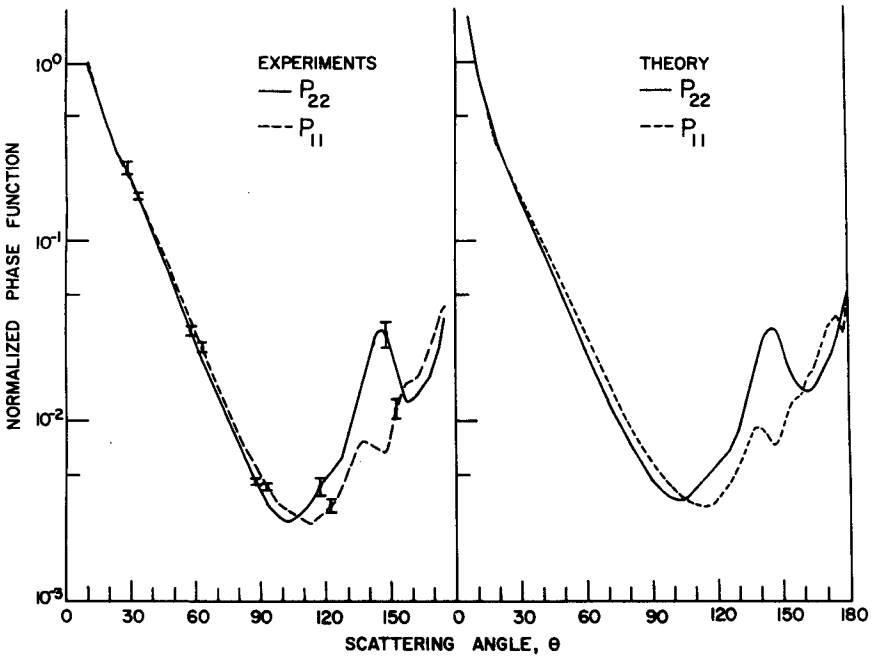

FIG. 3. A comparison of the normalized phase functions (divided by 4π) for incident vertically (P_{22}) and horizontally (P_{11}) polarized light from water cloud experiments and theory using the same cloud droplet size distribution. Experimental values are scaled to theoretical values at $\theta=10°$. Vertical bars show typical standard deviations of values averaged over five successive nephelometer scans.

proper alignment between the incident laser light plane of vibration and the orientation of the receiver polarizing prism. Prism alignment to better than 0.5° from the incident vertical or horizontal polarization directions is checked prior to experimentation, so that this error is no greater than 1% of the β_s values. A more significant source of uncertainty may result from fluctuations in cloud composition which would lead to angular variations in the β_s values which are unrepresentative of a homogeneous scattering medium. To reduce the impact of rapid, small-scale cloud variations, β_s values are averaged over 5° scattering angle intervals. In addition, when cloud samples and σ' values indicate little change in cloud composition

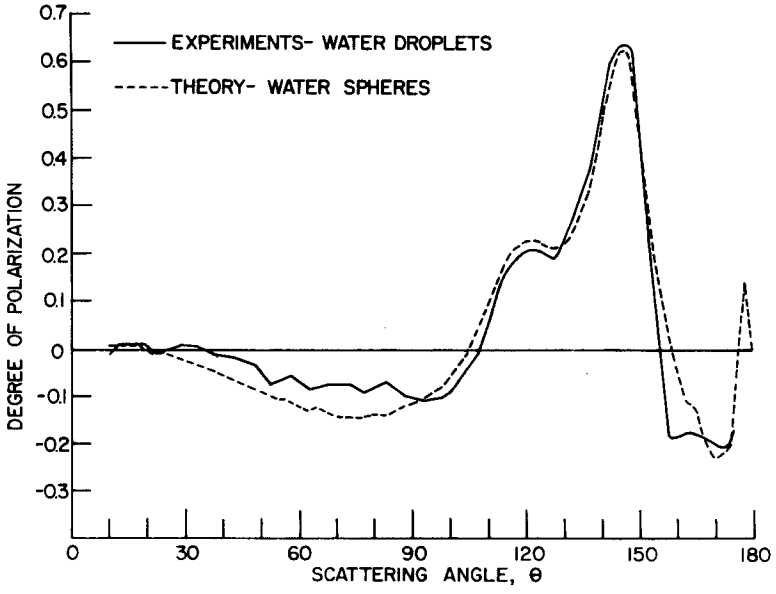

FIG. 4. A comparison of the degree of linear polarization parameter derived from the experimental and theoretical water cloud phase functions of Fig. 3.

over long time periods, several successive scans for each incident polarization state are normalized and averaged to obtain smoothed phase functions. Typical standard deviations of the averages obtained in this way are included for illustration in the experimental data plots to follow.

4. Experimental results

a. Water droplet clouds

With the availability of the cloud droplet size distributions collected with the sampling device during experimentation, it is possible to generate Mie scattering phase functions for a similar polydispersion of water spheres in order to permit a detailed comparison of the experimental and theoretical patterns. Fig. 3 presents such a comparison.

Shown in the left side of Fig. 3 are the normalized phase functions derived from measurements of a rather dense water cloud ($\sigma' = 1.5$ m^{-1}) for incident laser light polarized in the vertical (P_{22}, solid curve) and horizontal (P_{11}, dashed curve) directions. These curves represent the average of five normalized nephelometer scans which were then scaled to agree with theoretical predictions at $\theta = 10°$. Typical standard deviations of the averages are shown as vertical bars. Measurements obtained at the 10° and 175° terminations of the scans are also included in the figure. The measured cloud droplet size distribution displayed a modal diameter of 2 μm, a slight secondary peak at 6 μm and maximum diameters of 10 μm. This size spectra was fitted with the log-normal ZOLD distribution (see Kerker, 1969) with 2 μm modal diameter and a geometric mean standard deviation of 0.275 to generate the Mie scattering phase functions (Liou and Hansen, 1971) shown on the right side of Fig. 3. These phase functions and all others to follow are normalized with respect to 4π.

The comparison of the experimental and theoretical patterns derived under these conditions can be seen to yield rather close agreement. As a consequence of the relatively small size of the cloud droplets, both theory and measurement show that the secondary cloudbow is absent and that the primary cloudbow reaches a maximum at ~146°. The differences in phase functions for vertically (P_{22}) and horizontally (P_{11}) polarized light can be expressed quantitatively with the degree of linear polarization parameter LP, defined as

$$\mathrm{LP}(\theta) = \frac{P_{22}(\theta) - P_{11}(\theta)}{P_{22}(\theta) + P_{11}(\theta)}. \qquad (15)$$

Shown in Fig. 4 is the comparison of LP versus scattering angle θ for the experimental (solid line) and theoretical (dashed line) phase functions of Fig. 3. Close agreement is found in the vicinity of the primary cloudbow where strongly positive polarization values

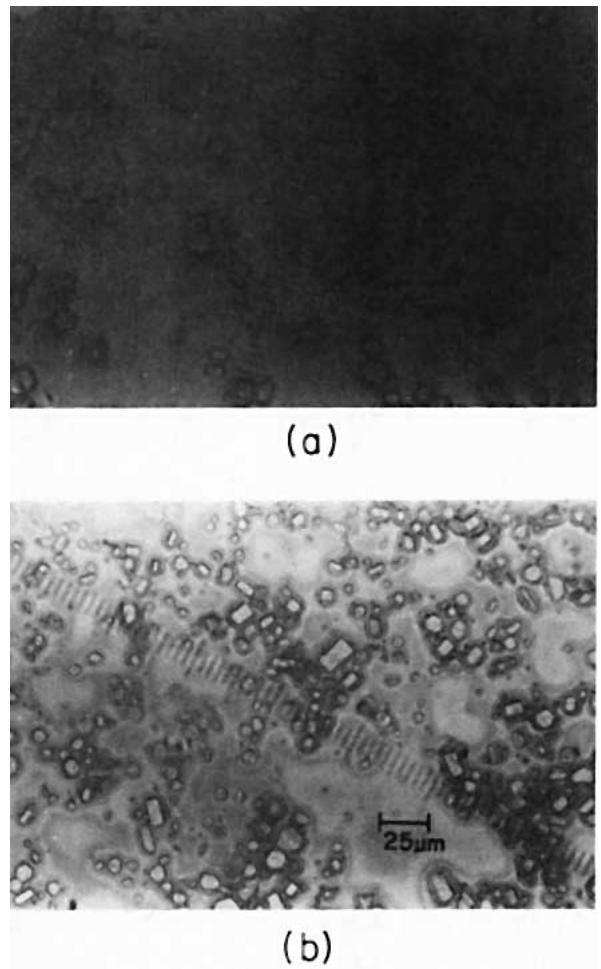

FIG. 5. Typical photomicrographs of ice crystal replicas obtained with the cloud sampling device used in the determination of the composition of two of the ice clouds described in the text.

are observed. It appears that the negative LP values in the scattering region from 30–90° are somewhat underestimated in the experimental data.

The favorable agreement between our water cloud measurements and theoretical predictions generated with actual size distribution inputs is encouraging. It seems to support the accuracy of our scattering and cloud composition measurements. Moreover, it also indicates that the effect of multiple scattering activity on the phase functions derived from our artificial clouds is not significant. The mutiple-scattering process in water clouds will be examined further in Part II of this report with the aid of depolarization measurements.

b. Ice crystal clouds

The prime objective of our program of ice cloud measurements has been to categorize the angular scattering behavior of atmospheric ice clouds, including an assessment of any dependence on crystal type and

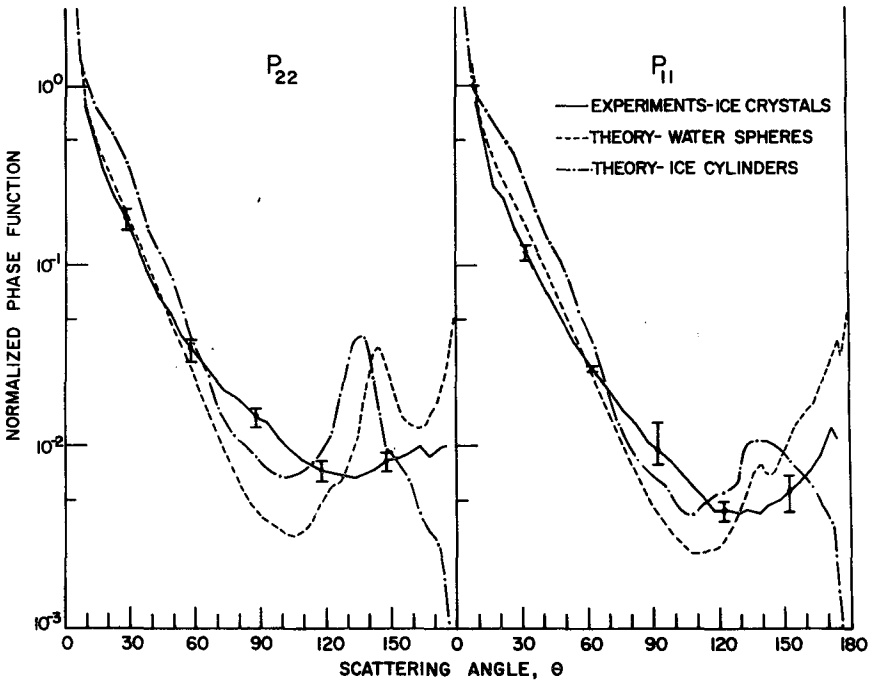

FIG. 6. Normalized phase functions derived from a representative ice cloud experiment compared with theoretical predictions for water spheres with the same size distribution and for infinitely long ice cylinders. Experimental values with standard deviations (vertical bars) are normalized to correspond to the values for spheres at $\theta = 10°$.

size, and to compare the results with available theoretical predictions for spherical and nonspherical particles. A basic limitation of laboratory studies, however, must be acknowledged in that it is not possible to reproduce the entire range of ice particle types and sizes which occur naturally due to the limited particle growth times achieved in the artificial cloud chamber environment. With the method of artificial cloud production employed in our experiments, it has also been found difficult to maintain pure-phase cloud conditions over acceptable time periods when relatively large ice crystals were present. Hence, most data have been obtained from stable ice clouds containing high concentrations of small crystals, generally from about 1.5–25 μm modal maximum dimensions. Crystal sizes seldomly exceeded 50 μm maximum dimensions, so that it can probably be assumed that the ice clouds contained exclusively randomly oriented particles. For illustration, we show in Fig. 5 two photomicrographs of crystal replicas from clouds described below.

Shown in Fig. 6 as the solid lines for vertically (P_{22}, left) and horizontally (P_{11}, right) polarized incident light are the normalized phase functions derived from measurements of an ice crystal cloud. These data have been chosen as being representative of the angular scattering behavior of the artificial ice clouds for the purpose of comparison to theoretical predictions. The experimental scattering patterns are each derived from averages of three scans alternatively obtained for each incident polarization state from a stable ice cloud, with the standard deviations of the averages given as vertical bars. The ice cloud contained simple and internally structured plate crystals displaying a log-normal size distribution with a modal maximum dimension (i.e., plate diameter) of 3.5 μm, a slight secondary peak at 20 μm, and maximum crystal sizes of about 30 μm (see solid curve in Fig. 9). The cloud generated by dry ice seeding at a temperature of $-12°$C was rather dense ($\sigma' = 1.85$ m^{-1}). Also included in Fig. 6 are the normalized phase functions derived from Mie theory for a polydispersion of water spheres (dashed lines) displaying a very similar size distribution as the ice cloud, and for a monodispersed assembly of randomly oriented ice cylinders (dash-dotted lines) of infinite length and 10 μm circular radius (Liou, 1972).

In comparison to the angular scattering behavior of spherical cloud droplets, the ice crystal cloud can be seen to generate more intense side scattering and to lack the cloudbow maximum. The results obtained using the cylindrical shape approximation display stronger side scattering than spherical particles, and so are more appropriate for comparison to the ice crystal cloud data in this region. However, both spheres and cylinders generate cloudbows due to their circular geometric cross sections. It is also apparent that the randomly oriented ice cylinders produce very weak backscattering. Due to the presence of the glory for the water spheres at $\theta \approx 180°$, the water cloud

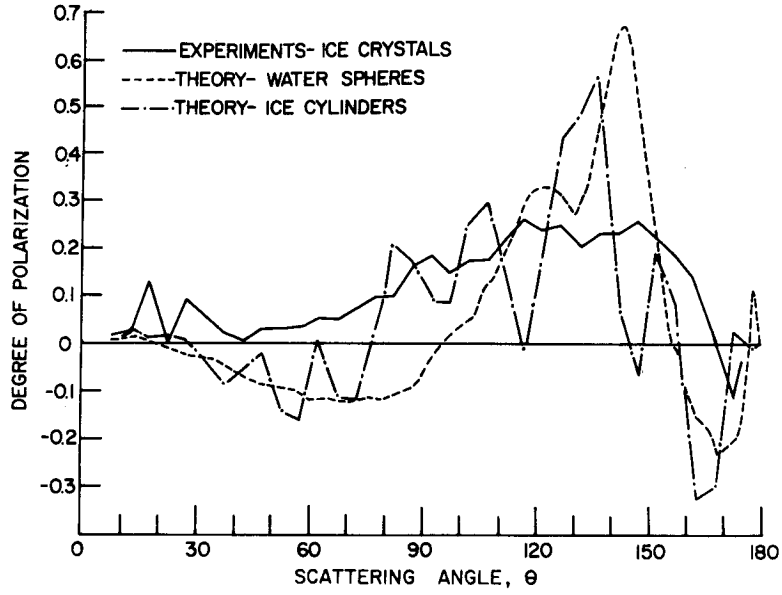

FIG. 7. Degree of linear polarization parameter corresponding to the three cases shown in Fig. 6.

phase function displays a sharp increase in approaching true backscattering. This feature, however, would not likely be present in the ice cloud pattern if measurements were available in the 175–180° scattering interval due to the absence of the glory for irregular particles.

The degree of polarization calculated from Eq. (15) is shown in Fig. 7 for the three cases discussed above. In contrast to the results for both spheres and cylinders, the experimental ice data generally lack negative polarization values. Negative polarization is typically observed only in approaching the backscatter, and also often in the region of the 22° halo when relatively large ice crystals are present, as expected from observations of the solar 22° halo (Meyer, 1929). Although the ice cylinder values display fluctuations resulting from intensity maximum and minimum associated with the use of a monodispersed population, they appear to provide better agreement than the results from spheres.

While the experimental scattering pattern described above can be used to categorize our data from ice

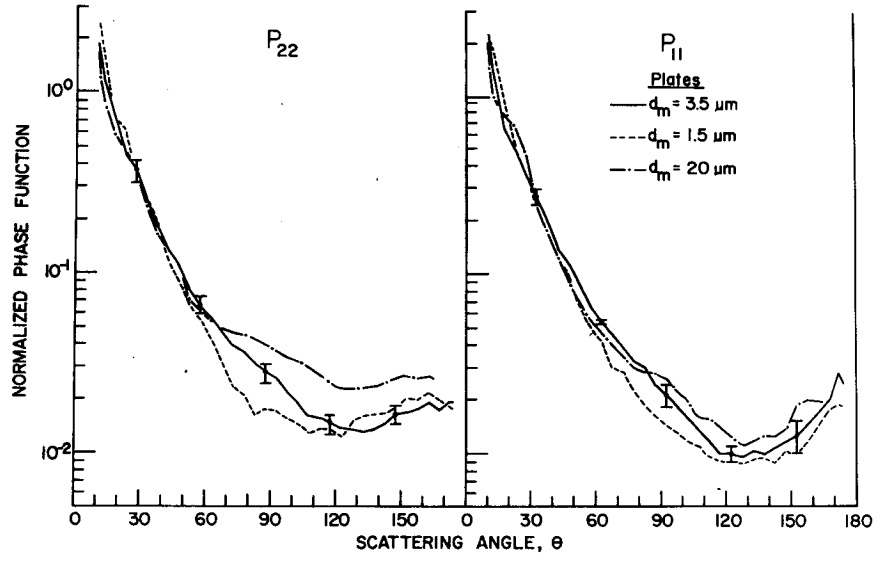

FIG. 8. Experimental scattering patterns for incident vertically (P_{22}) and horizontally (P_{11}) polarized light for three ice clouds containing plate crystals with the indicated modal maximum dimensions (d_m). Typical standard deviations are illustrated for one of the experiments.

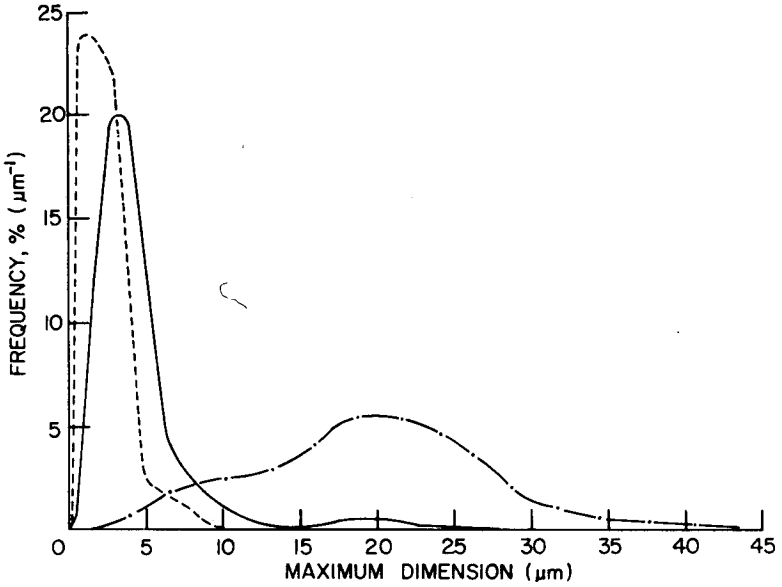

FIG. 9. The relative size distributions of the plate crystal maximum dimensions corresponding to the phase functions of Fig. 8.

clouds, certain aspects of the angular scattering behavior of ice crystals are indicated to be influenced by particle size and shape. Examining first the effect of ice crystal size, shown in Fig. 8 in the form used earlier are the phase functions normalized with Eq. (14) for three artificial clouds containing exclusively plate crystals. As can be seen from the corresponding particle size distributions depicted in Fig. 9, the three clouds had modal maximum dimensions of 1.5, 3.5 and 20 μm, with extinction values of $\sigma' = 1.0$, 1.85 and 0.55 m^{-1}, respectively. In these patterns for uniformly shaped particles, the effects of increasing crystal size appear to be manifested primarily in increased side scattering in the θ interval from about 60–160°. In the forward-scattering direction there is a tendency for the 22° halo to become increasingly prominent for the larger particles. The experimental results suggest, on the other hand, that ice cloud backscattering is not as sensitive to particle size.

Fig. 10 shows in a similar manner the influence of ice crystal shape on scattering properties. The corresponding particle size distributions given in Fig. 11

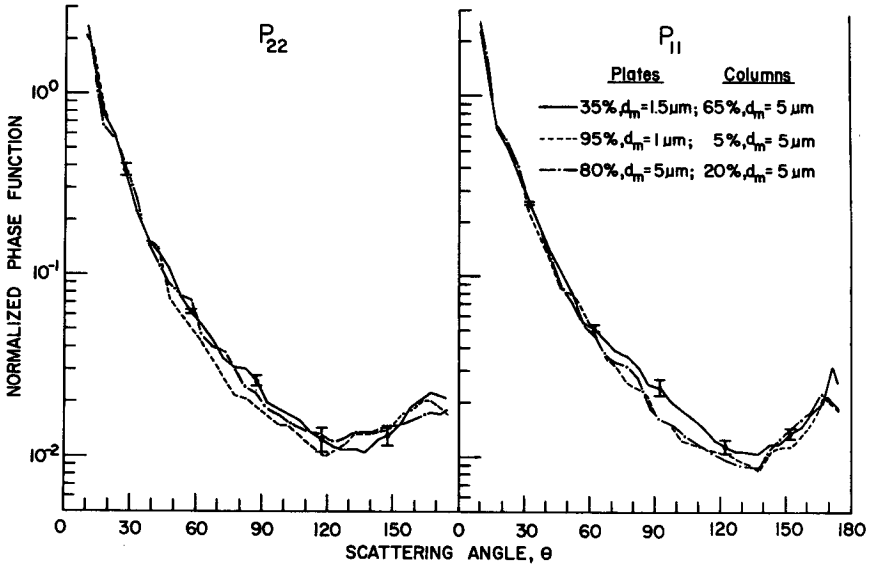

FIG. 10. Experimental scattering patterns for three ice clouds showing the effects of ice crystal type. Given in the key are the relative frequency of occurrence (%) and modal maximum dimensions (d_m) of the plate and column ice crystals present in each cloud.

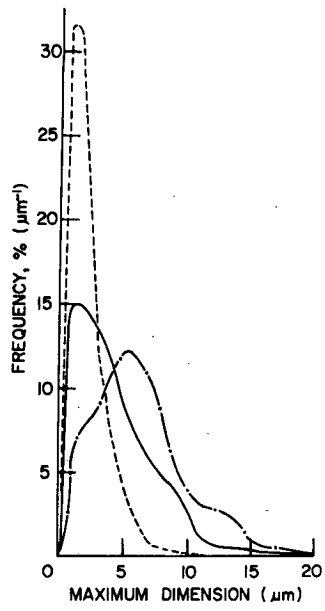

FIG. 11. The relative size distributions of the ice crystal maximum dimensions corresponding to the phase functions of Fig. 10.

display modal maximum dimensions ranging from 1.0 to 5.0 μm, with the following characteristics: dashed curve—95% 1 μm mode plates, 5% 5 μm mode solid columns ($\sigma'=0.75$ m^{-1}); dash-dotted curve (see Fig. 5a)—80% plates and 20% short columns both with 5 μm modes ($\sigma'=0.85$ m^{-1}); and solid curve (see Fig. 5b)—35% 1.5 μm mode plates and thick plates and 65% 5 μm mode columns ($\sigma'=2.0$ m^{-1}). In these data, the cloud containing the highest percentage of columnar crystals (solid curves) displays the tendency for the greatest side-scattering efficiency, despite the fact that the dash-dotted curves represent a cloud containing larger particles. Thus, side-scattering efficiency also appears to be influenced by ice crystal habit. This may be due to the fact that thin plate crystals lack the large prismatic face areas of columnar crystals which would promote more intense internal reflections (Sassen, 1977).

c. *Mixed-phase clouds*

From the preceding sections, it can be concluded that the major differences in the angular scattering patterns for water and ice clouds are in the presence of water and ice particle optical phenomena, and in the difference in particle side-scattering efficiencies. When both water and ice particles are present in a mixed-phase cloud environment, as is very frequently the case in atmospheric clouds, a mixture of the features of the angular scattering patterns for the particles in the two phases will be produced. The angular scattering properties of this important cloud group have been studied by performing successive nephelometer scans of a pure water cloud which was then glaciated through dry-ice seeding, and subsequently allowed to become mixed phase with gradu-

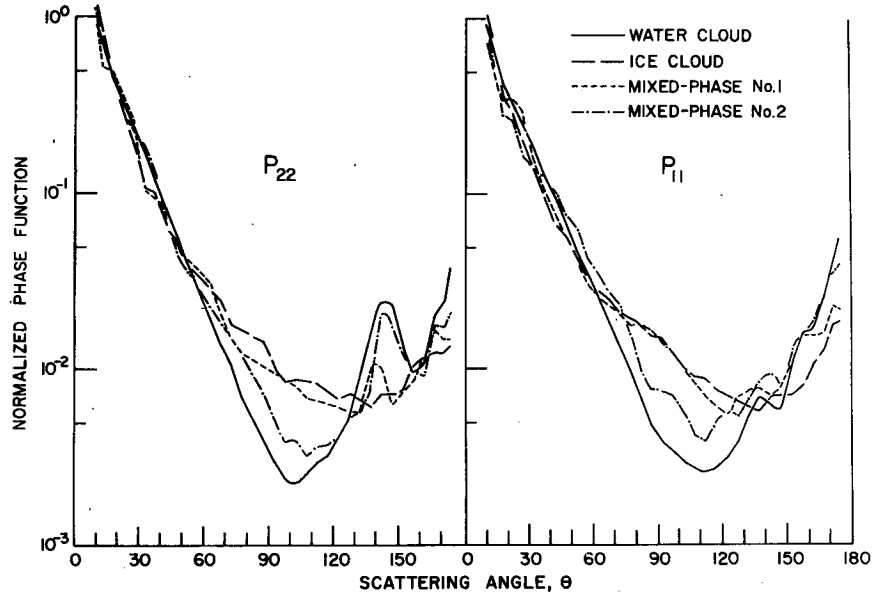

FIG. 12. Normalized phase functions derived from successive, single scans illustrating the distinct scattering behavior of mixed phase clouds and the significant differences in pure water and ice clouds. Data labeled Mixed-Phase No. 1 and No. 2 represent cloud conditions dominated by ice and water particles, respectively. Pure water cloud data are normalized at $\theta=10°$ to correspond to theoretical predictions, with the other curves scaled by this same factor.

ally increasing amounts of liquid water. Fig. 12 presents the results of such an experiment, and also illustrates the significant differences in the normalized phase functions for pure water and pure ice clouds.

Prior to seeding the cloud at a cold chamber temperature of −8.5°C a rather narrow cloud droplet distribution with a 1.5 μm modal diameter was present. The phase transition produced a dense cloud of columnar and thick plate crystals ranging from about 1–20 μm in maximum dimension, with a modal value of 3 μm. With the onset of mixed phase conditions, relatively large cloud droplets were initially detected and the size distribution of the ice crystals was noted to broaden. Values of $\sigma' \approx 1.5$ m^{-1} were measured in the water and mixed-phase states, and 2.0 m^{-1} in the pure ice phase.

The normalized phase functions obtained under these conditions are shown for vertically (P_{22}) and horizontally (P_{11}) polarized incident light on the left and right sides of Fig. 12, respectively. After each curve was normalized with the aid of Eq. (14), the water cloud data were scaled in such a way that the phase functions obtained from the experiments and Mie theory were in agreement at $\theta = 10°$. The other experimental patterns for the ice and mixed-phase clouds were scaled by the same factor for this comparison. Each pattern is identified in the figure according to the phase of the cloud, with the data labeled as Mixed Phase No. 1 and No. 2 representing cloud compositions first dominated by ice crystals and then by the droplet constituents. The size distribution of the droplets and ice crystals obtained from a cloud sample at the completion of the Mixed Phase No. 1 scans is given in Fig. 13 where the droplets can be seen to have comprised ~25% of the total particle count at that time. Note that since no averaging of the scattered intensities can be performed under these changing cloud conditions, the patterns display some irregularities induced by cloud microstructure fluctuations in the scattering volume.

A comparison of the normalized patterns for the pure water and ice phases yields the anticipated results: ice crystal scattering is considerably stronger near 90°, and weaker from roughly 20–50°, and in the backscatter. The prominent cloudbow centered at 145° also clearly differentiates the scans for vertically polarized light. In accordance with these dissimilarities in the scattering patterns for pure water and ice clouds, the relative differences in angular scattering efficiency have a significant impact on the mixed-phase cloud scattering pattern. It is evident from Fig. 12, for example, that even relatively small amounts of droplets in a primarily ice cloud (dashed line) cause cloudbows to protrude above the ice cloud side scattering, whereas under the reverse conditions (dash-dotted line) the presence of a small ice component is still indicated by elevated side scattering. With increasing relative water content, backscattering

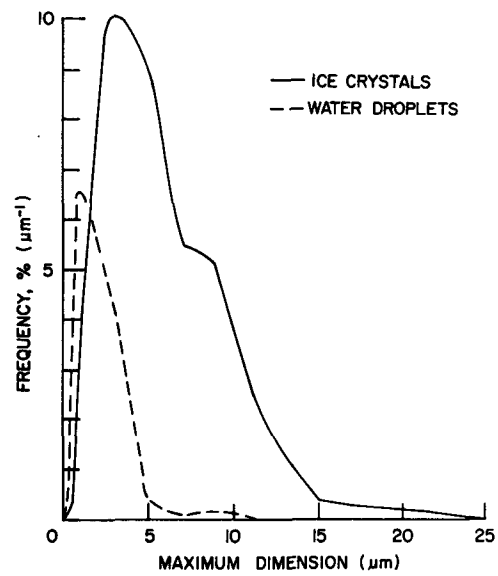

FIG. 13. Relative size distributions of the water droplets and ice crystals obtained between the Mixed Phase No. 1 and No. 2 scans of Fig. 12.

and forward scattering tend to increase as would be expected in response to the greater scattering efficiencies of droplets in these regions.

The characteristics of the optical phenomena present in the mixed-phase cloud data also provide some information on cloud composition which is supported by the cloud samples. The generally increased prominence of the 22° ice crystal halo indicates larger particles to be present in the mixed-phase cloud due to the more rapid growth rate achieved by ice at water saturation in comparison to glaciated conditions. And, interestingly, the cloudbow can be seen to be centered at ~140° in Mixed Phase No. 1 when droplets initially began to coexist with the ice crystals. This shift from the ~145° positions observed both before and after indicates that the first liquid elements to be reintroduced into the ice cloud were of larger diameter.

5. Discussion and summary

Significant differences in the angular scattering behavior of water and ice clouds have been demonstrated for artificial clouds composed of ice crystals and cloud droplets with maximum dimensions $\lesssim 50$ and 10 μm, respectively. These differences induced by particle shape effects are manifested by 1) stronger ice cloud side scattering in the region from about 60–130°, 2) stronger water cloud scattering in the forward direction from 10–60° and in the backscatter for $\theta > 160°$, and 3) the presence of optical phenomena such as cloudbows and haloes which also clearly distinguish the angular scattering patterns of water and ice clouds. The scattering patterns for mixed phase

TABLE 1. Experimental phase function values for a representative ice crystal cloud scaled with reference to the normalized phase function for spheres at scattering angle $\theta=10°$, for parallel and orthogonal polarization measurements with incident vertically (i.e., P_{22} and P_{12}) and horizontally (i.e., P_{11} and P_{21}) polarized light, and for unpolarized light with the depolarized components neglected $[(P_{11}+P_{22})/2]$ and included $[(P_{11}+P_{22})/2+(P_{12}+P_{21})/2]$.

θ(°) (deg)	P_{22}	P_{12}	P_{11}	P_{21}	$(P_{11}+P_{22})/2$	$(P_{11}+P_{22})/2$ + $(P_{12}+P_{21})/2$
0*	1.15+2	0	1.15+2	0	1.15+2	1.15+2
2.5*	2.13+1	0	2.13+1	0	2.13+1	2.13+1
5*	3.29+0	0	3.30+0	0	3.30+1	3.30+0
7.5*	1.33+0	0	1.34+0	0	1.34+0	1.34+0
10	7.74−1	1.70−3	7.70−1	1.39−3	7.72−1	7.74−1
15	4.88−1	1.32−3	4.04−1	8.48−4	4.46−1	4.47−1
20	3.23−1	1.03−3	2.52−1	6.55−4	2.87−1	2.88−1
25	2.16−1	8.25−4	1.78−1	5.34−4	1.97−1	1.98−1
30	1.51−1	7.10−4	1.34−1	4.82−4	1.43−1	1.43−1
35	1.08−1	6.26−4	1.00−1	4.30−4	1.04−1	1.05−1
40	7.87−2	5.67−4	7.57−2	4.01−4	7.72−2	7.77−2
45	6.02−2	5.42−4	5.82−2	3.78−4	5.92−2	5.97−2
50	4.72−2	5.19−4	4.45−2	3.56−4	4.59−2	4.63−2
55	3.81−2	5.33−4	3.52−2	3.48−4	3.67−2	3.71−2
60	3.12−2	5.30−4	2.85−2	3.56−4	2.99−2	3.03−2
65	2.59−2	5.57−4	2.31−2	3.70−4	2.45−2	2.50−2
70	2.18−2	6.00−4	1.89−2	3.87−4	2.04−2	2.08−2
75	1.90−2	6.56−4	1.60−2	4.32−4	1.75−2	1.80−2
80	1.69−2	7.44−4	1.37−2	4.80−4	1.53−2	1.59−2
85	1.52−2	8.21−4	1.18−2	5.37−4	1.35−2	1.42−2
90	1.35−2	9.18−4	1.01−2	5.86−4	1.18−2	1.26−2
95	1.18−2	1.00−3	8.53−3	6.31−4	1.02−2	1.10−2
100	1.02−2	1.07−3	7.22−3	6.86−4	8.71−3	9.59−3
105	8.93−3	1.16−3	6.08−3	7.30−4	7.51−3	8.45−3
110	8.02−3	1.24−3	5.28−3	8.18−4	6.65−3	7.68−3
115	7.43−3	1.37−3	4.74−3	8.77−4	6.09−3	7.21−3
120	7.04−3	1.51−3	4.32−3	9.29−4	5.68−4	6.90−3
125	6.83−3	1.64−3	4.12−3	9.89−4	5.48−3	6.79−3
130	6.62−3	1.82−3	4.11−3	1.13−3	5.37−3	6.84−3
135	6.67−3	2.00−3	4.21−3	1.26−3	5.44−3	7.07−3
140	7.10−3	2.43−3	4.41−3	1.46−3	5.76−3	7.65−3
145	7.68−3	2.65−3	4.72−3	1.63−3	6.20−3	8.34−3
150	8.32−3	2.91−3	5.19−3	1.82−3	6.76−3	9.12−3
155	8.75−3	3.06−3	5.83−3	1.79−3	7.29−3	9.83−3
160	9.02−3	3.11−3	6.78−3	2.10−3	8.19−3	1.05−2
165	9.28−3	3.16−3	8.00−3	2.00−3	8.64−3	1.12−2
170	9.55−3	3.20−3	9.72−3	1.94−3	9.64−3	1.22−2
175	9.77−3	3.32−3	1.07−2	2.46−3	1.02−2	1.31−2
180†	1.01−2	5.05−3	1.01−2	5.05−3	1.01−2	1.52−2

* Values calculated from Mie theory for a population of water spheres with the same size distribution as the ice crystal maximum dimensions.

† Values estimated, see text.

clouds strongly depend on these relative angular scattering efficiencies as well as cloud water-ice balance.

With regard to the effect that ice cloud composition has on the experimental scattering patterns, we have found evidence that ice cloud side scattering tends to increase with increasing crystal size. This tendency is opposite to the behavior of water clouds (Liou and Hansen, 1971), showing that the differences in angular scattering behavior induced by particle shape effects become more significant in approaching the geometrical optics scattering domain, while decreased sensitivity to particle shape is experienced when the particle size and wavelength are of about the same order. Similarly, the characteristics of the optical phenomena present in the scattering patterns are also indicated to depend on particle phase and size. On the basis of our observations, ice crystal maximum dimensions on the order of 20 μm appear to delineate the lower limit of ice crystal sizes responsible for halo formation. (A review of earlier laboratory studies in which haloes were and were not present also supports this approximate threshold particle size.) Since much smaller cloud droplets can generate strong cloudbows, it can be argued that the ray tracing method is less applicable to nonspherical particles than to spheres when the particle sizes are only slightly greater than the incident wavelength.

With the knowledge of the cloud particle size distribution present during experimentation, detailed comparisons of the phase functions derived from measurements and Mie theory simulations have been made possible. For water droplet clouds, good agreement has found between experiments and theory when the actual droplet size distribution was input into the computations. For ice crystal clouds of either planar or prismatic habit, the agreement between the measurements and theory using the long cylinder shape approximation is less noteworthy. Discrepancies are particularly apparent in the presence of inappropriate cloudbows and significantly reduced backscattering in the theoretical results. Hence, considerable errors may arise by treating ice-containing clouds with theory using either the long cylinder or spherical shape approximations. Theoretical analyses involving finite hexagonal particles are clearly required to explain physically the scattering behavior of ice clouds.

The examples provided here for the phase functions of pure ice and mixed-phase clouds can find application in radiative transfer calculations through many kinds of cloudy atmospheres. In order that these data can be more readily applied to such simulations, the tabulated phase function values for an ice cloud chosen as being representative of our data (from Fig. 6) are given in Table 1. Included in the table are normalized phase function values (divided by 4π) at successive 5° scattering angle positions for incident vertically (P_{22}) and horizontally (P_{11}) polarized light, and for unpolarized light [i.e., $(P_{11}+P_{22})/2$]. The original data have been smoothed to remove slight irregularities in the patterns and normalized by adjusting the experimental values so that the phase function value at $\theta=10°$ corresponded to the value computed for a population of spheres with the same size distribution as the crystal maximum dimensions. Hence, values from Mie theory for spheres have been given at the 0, 2.5, 5 and 7.5° scattering angles in the table as an approximation of the ice cloud forward scattering. As an additional approximation, phase function values at $\theta=180°$ were derived by taking the average value at $\theta=175°$ for the two incident polarization states. Since the glory would be absent

in ice crystal backscattering, a strong increase at 180° is unlikely. The use of these procedures, then, permits the construction of a normalized phase function appropriate for our ice crystal clouds of randomly oriented hexagonal particles over the entire 180° scattering angle range, as compiled in Table 1.

Also given in Table 1 are additional phase function values which represent the contributions from the depolarized components of the scattered laser light. As will be described in Part II, ice crystal clouds can produce considerable depolarization of the incident light at some scattering angles as a consequence of particle shape effects. Thus, unlike the case for spherical scatterers, the additional energy contained in the depolarized components must be considered in adapting the experimental ice cloud phase functions for radiative transfer calculations. The required information is compiled in the table in the form of phase function values for orthogonal polarization with vertically (P_{12}) and horizontally (P_{21}) polarized incident light, and for unpolarized incident light calculated with the inclusion of these depolarized components $[(P_{11}+P_{22})/2+(P_{12}+P_{21})/2]$. As approximations, it has been assumed that no depolarization was generated for $\theta<10°$, while at $\theta=180°$ a linear depolarization ratio of 0.50 was used on the basis of earlier studies (Sassen, 1974).

Finally, some discussion of the limitations of the phase function values of Table 1 for radiative transfer purposes is in order. We have attempted to provide in Table 1 a complete phase function which is representative of assemblies of small, randomly oriented ice crystals. Clearly, atmospheric ice clouds may contain in addition to such crystals a large variety of ice particle types and sizes. A further complication arises from the fact that large ice crystals can maintain uniform orientations in space, so that the scattering properties develop a dependence on the incoming solar radiation angle. Natural ice particles can also quite frequently be comprised of combinations of hexagonal crystal elements, resulting in particles of complex shape which do not orient uniformly in space. The recent nephelometer measurements by Dugin *et al.* (1977) in a large cold chamber indicate, however, that such complex particles produce scattering patterns which are very similar to those for randomly oriented, simple crystals. Thus, except where large, preferentially oriented ice crystals are present, it would appear that the data contained in Table 1 can be used to categorize the behavior of many kinds of atmospheric ice clouds to a much better approximation than can be obtained through present theoretical approaches. In order to bring our comprehension of ice cloud angular scattering behavior to the level currently afforded to the treatment of water droplet clouds, what appears to be needed in view of these complexities is a combination of experimental studies of realistic cloud compositions and theoretical simulations for finite hexagonal ice particles of specified aspect and orientation.

Acknowledgments. This research was supported by the Atmospheric Research Section of the National Science Foundation under Grant ATM 75-05216. We thank S. P. Hunter and P. Flatt for their assistance in various aspects of the experimental program.

REFERENCES

Dugin, V. P., B. M. Golubitskiy, S. O. Mirumyants, P. I. Paramonov and M. V. Tantashev, 1971: Optical properties of artificial ice clouds. *Izv. Atmos. Ocean. Phys.*, **7**, 871–877.

——, O. A. Volkovitskiy, S. O. Mirumyants and N. K. Nikiforova, 1977: Anisotropy of light scattering by artificial crystalline cloud formations. *Izv. Atmos. Ocean. Phys.*, **13**, 22–25.

Holland, A. C., and G. Gagne, 1970: The scattering of polarized light by polydisperse systems of irregular particles. *Appl. Opt.*, **9**, 1113–1121.

Huffman, P., 1970: Polarization of light scattered by ice crystals. *J. Atmos. Sci.*, **27**, 1207–1208.

——, and W. R. Thursby, 1969: Light scattering by ice crystals. *J. Atmos. Sci.*, **26**, 1073–1077.

Jacobowitz, H., 1970: Emission, scattering and absorption of radiation in cirrus cloud layers. Ph.D. thesis, M.I.T., 181 pp.

Kerker, M., 1969: *The Scattering of Light and Other Electromagnetic Radiation.* Academic Press, 666 pp.

Liou, K. N., 1972: Light scattering by ice clouds in the visible and infrared: A theoretical study. *J. Atmos. Sci.*, **29**, 524–536.

——, 1975: Theory of the scattering-phase-matrix determination for ice crystals. *J. Opt. Soc. Amer.*, **65**, 159–162.

——, and J. E. Hansen, 1971: Intensity and polarization for single scattering by polydisperse spheres: A comparison of ray optics and Mie theory. *J. Atmos. Sci.*, **28**, 995–1004.

——, R. Baldwin and T. Kaser, 1976: Preliminary experiments on the scattering of polarized laser light by ice crystals. *J. Atmos. Sci.*, **33**, 553–557.

Meyer, R., 1929: Die haloersheinungen. *Probl. Kosmich. Phys.*, **12**, 19–21.

Perrin, F., 1942: Polarization of light scattered by isotropic opalescent media. *J. Chem. Phys.*, **10**, 414–427.

Platt, C. M. R., 1973: Lidar and radiometric observations of cirrus clouds. *J. Atmos. Sci.*, **30**, 1191–1204.

Sassen, K., 1974: Depolarization of laser light backscattered by artificial clouds. *J. Appl. Meteor.*, **13**, 923–933.

——, 1977: Ice crystal habit discrimination with the optical backscatter depolarization technique. *J. Appl. Meteor.*, **16**, 425–431.

——, 1978a: Backscattering cross sections for hydrometeors: measurements at 6328 Å. *Appl. Opt.*, **17**, 804–806.

——, 1978b: The continuous-impactor-replicator for laboratory cloud composition analysis. *J. Appl. Meteor.*, **17**, 1319–1326.

——, and K. N. Liou, 1978: Angular scattering of polarized laser light by water droplet and ice crystal clouds. *Preprints Third Conf. Atmospheric Radiation*, Davis, Amer. Meteor. Soc., 95–99.

——, and ——, 1979: Scattering of polarized laser light by water droplet, mixed phase, and ice crystal clouds. Part II: Angular depolarizing and multiple scattering behavior. *J. Atmos. Sci.*, **36**, 852–861.

van de Hulst, H. C., 1957: *Light Scattering from Small Particles.* Wiley, 471 pp.